

Light Load Efficiency Improvement for Three-Phase Inverter Employing Variable Switching Frequency Control under Mixed TCM/DCM Operation

Jie Deng, Jianliang Chen, *Member, IEEE*, Zhen Xin, *Member, IEEE*

Abstract– In this paper, A variable switching frequency control under mixed triangular conduction mode/discontinuous conduction mode (TCM/DCM) operation is proposed to improve the light load efficiency for three-phase inverter. Zero voltage switching (ZVS) can be achieved easily at full range load under triangular conduction mode (TCM) operation, but the efficiency drops rapidly at light load due to the increasing switching frequency. Therefore, discontinuous conduction mode (DCM) with the variable switching frequency control is adopted to limit the switching frequency under TCM. The optimum changing modulation point for the best overall efficiency performance is presented based on the loss analysis under single TCM and DCM operation, respectively. Meanwhile, no matter whether under TCM or DCM, consistent valley switching (VS) can be achieved to reduce switching losses at any load or modulation index without any additional sensors, auxiliary circuits, or current zero-crossing detection (ZCD) circuits. A 3.3 kW experimental prototype interfacing a 400 V dc with three-phase 110 V ac is developed to verify the proposed control, which improves the light load efficiency by 0.55% to 3.9%.

Index Terms– light load efficiency, triangular conduction mode (TCM), discontinuous conduction mode (DCM), optimum changing modulation point, valley switching (VS), zero voltage switching (ZVS).

I. INTRODUCTION

The demands of the three-phase voltage source inverter (VSI) for higher conversion efficiency and power density never stop. Owing to the emerging wide bandgap (WBG) devices in recent years, the inverter performance is pushed forward which can operate at higher switching frequency. However, the switching loss is still significant at hundreds of kHz. Although the peak efficiency of most commercial products exceeds 98%, and some even reach 99%, the power density is still disappointing due to the general switching frequency (around 50 kHz) using SiC devices. Therefore, the switching frequency should be improved to fully utilize the high-speed switching characteristics of SiC MOSFETs. It can be concluded from the double pulse test that the turn-on loss of the SiC MOSFET is much higher than the turn-off loss [1]. Therefore, zero voltage switching (ZVS) technique can be used to significantly improve the switching frequency, efficiency, as well as power density.

In the past few years, there have been many studies on soft-switching techniques applied to three-phase VSIs. To achieve

ZVS for both switches in a phase-leg, the inductor current must flow into the middle point before the top switch is turned on and flow out before the bottom switch is turned on. The most ZVS techniques need auxiliary circuits to inject an additional current into the middle point, so the direction of the total current can be changed. According to the positions of the auxiliary circuits, they can be classified into resonant dc-link (RDCL) inverters [1]–[3] and auxiliary resonant commutated pole (ARCP) inverters [4]–[6]. They can achieve a wide range of soft switching of main switches as well as auxiliary switches. However, the additional resonant cell may complicate the control strategy and introduce extra size, cost, and power loss.

To eliminate the auxiliary circuits, an intuitive way is to increase the inductor current ripple so that the current can change its direction in a switching cycle. Triangular conduction mode (TCM) is deemed as one of the most attractive solutions for high power density with high frequency, which has been implemented in bidirectional buck-boost converters [7], totem-pole bridgeless power factor correction (PFC) rectifiers [8], and single-phase inverters [9], [10]. To minimize the unnecessary current ripple and circulation loss, the switching frequency is taken as another control degree of freedom. Meanwhile, based on current ripple prediction, any additional sensors and current zero-crossing detection (ZCD) can also be eliminated under TCM operation. It can also distribute the conducted EMI spectrum and effectively reduce the EMI filter size [11].

For the three-phase inverter, it is more difficult to achieve ZVS for all the switches because the three-phase currents are tightly coupled. The summation of the three-phase currents is always zero. Moreover, the switching state of any phase-leg affects the current ripple of every inductor. Due to these coupling factors, it is very complicated to control the inductor current ripple in three phases simultaneously. To overcome this issue, some studies are presented [11]–[18]. According to the Circuit topology, they can be clarified either on the modulation decoupling or the hardware decoupling. For the modulation decoupling [11]–[15], the discontinuous pulse width modulation (DPWM) is adopted to ensure that only two phase-legs are switching at high frequency, while the other phase-leg is not switching, and is clamped to the positive or negative dc-bus at any time instant. Therefore, only two-phase inductor currents are controlled to achieve ZVS. However, the modulation method is limited (DPWM is necessary). For hardware decoupling [16]–[19], one method is by splitting

capacitors at the dc bus and connecting the neutral-point dc bus (O) to the ac side (N_1 and N_2), as Fig. 1 shows. Therefore, TCM operation analysis can be performed independently among three phases. However, the modulation ratio is limited (<1), and the ac side (N_2) is generally not available. The other method is only by connecting the neutral-point dc bus (O) to the ac side (N_1), which boosts the modulation ratio by 15% and transforms the sixth-order circuit into the pseudo-second-order circuit. Therefore, TCM can also operate independently. In this paper, the hardware method which connects the neutral-point dc bus (O) to the ac side (N_1) is adopted to decouple the three-phase current, as Fig. 1 (a) shows.

Regardless of the decoupling method, TCM operation also suffers from the switching frequency range over the line cycle and the sharp decline in efficiency as the load becomes lighter, which limits its practical application. These troublesome problems have common reasons that the switching frequency increases sharply at light loads or near the zero crossing of load current. Meanwhile, for some applications such as PV inverters, the light load efficiency is as crucial as the heavy load efficiency due to a term called “weighted efficiency” [20]. This applies weighting factors to various output powers by considering the operating profile of the inverter during the daytime. Hence, the light load efficiency must be improved.

However, the light load efficiency improvement for three-phase inverters has been rarely studied. For single-stage inverters, the phase skipping control is widely discussed in [21]–[24], in which the inverter is intermittently operated at light loads. However, their overall switching frequencies are all below 50 kHz, which is not good for the improvement of power density. Increasing the inductor ripple to achieve ZVS and limit switching frequency at light loads or near the zero crossing of load current is adopted in [25]. However, the conduction and switching losses of the switching devices increase significantly due to the large current ripple, which limits the high-power applications. In [26], phase shedding control is proposed to ameliorate the light load efficiency. However, this method cannot be directly applied to the single-stage three-phase inverter due to the missing control degree of freedom of another channel.

In this paper, a variable switching frequency control under mixed TCM/DCM operation for three-phase inverter without any auxiliary circuits or additional sensors is proposed to improve the light load efficiency. Compared to the TCM, DCM has excellent performance at light loads [27] [28], which can be controlled with a constant switching frequency. Meanwhile, with the variable switching frequency control under DCM operation, zero current switching (ZCS) turn-on, ZVS turn-off, and valley switching (VS) can be achieved to reduce the switching loss further. Therefore, the switching frequency range can be narrow, and the light load efficiency can be higher to combine the advantages of TCM and DCM. Meanwhile, the optimum tradeoff between load current and efficiency is determined by analyzing the power losses of the single TCM and DCM in order to explore the optimum changing modulation point (changes from TCM to DCM) to maximize efficiency. This paper is organized as follows. The conventional operation

of single TCM and DCM are investigated in Section II. The variable switching frequency control under DCM operation is explained in Section III. Based on the power loss analysis, the proposed mixed TCM/DCM operation is presented in Section IV. The detailed design consideration is discussed in Section V. The simulation and experimental verification are presented in Section VI. Finally, Section VII concludes this article.

II. OPERATION ANALYSIS OF SINGLE TCM AND DCM

The three-phase two-level inverter with an LCL filter configuration is shown in Fig. 1 (a). L is the inverter-side inductor. C is the filter capacitor and L_g is the grid side inductor. The inductor currents on the inverter side and the grid side are i_x ($x = a, b, c$) and i_{gx} respectively. V_{dc} is the dc voltage, and v_x are the three-phase voltage. Q_{1x} and Q_{2x} are the two switches of each phase. The gate signals of Q_{1x} and Q_{2x} are complementary. D_{1x} and D_{2x} are the diodes of two switches in each phase.

Because the inductor current ripple is influenced by the three-phase switching actions, the neutral-point of the ac filter capacitor is connected to the neutral-point dc-bus to decouple the three phases. Therefore, the following TCM and DCM operation analysis can be performed independently among three phases, and the sixth-order circuit in Fig. 1 (a) can be simplified as the pseudo-second-order circuit, as Fig. 1 (b) shows. Because the interval time in a switching cycle is too small, the grid voltage v_x is deemed as constant in a switching cycle. Besides, the current ripple of i_{gx} and the line frequency reactive current generated by the filter capacitors are neglected. Therefore, the assumption that the average inductor current of i_x in a switching cycle is equal to the instantaneous grid current i_{gx} can be given.

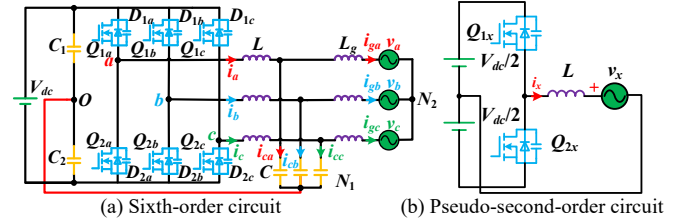


Fig. 1. Three-phase two-level inverter.

A. Single Conventional TCM Operation Analysis

Taking phase a whose load current is above 0 as an example, the inductor current waveform and the different intervals within a switching cycle are shown in Fig. 2. During interval 1, Q_{1a} is conducted and the inductor current i_a increases linearly. At t_0 , the inductor current i_a is equal to the desired current upper-level i_{a_up} . Q_{1a} is turned off, then the output capacitors C_{oss} of Q_{1a} and Q_{2a} are charged and discharged, respectively. During interval 2, The output capacitors C_{oss} of Q_{2a} is fully discharged to zero and the parasitic diode D_{2a} is conducted at t_1 . So Q_{2a} can be turned on between t_1 (minimum dead time) and t_2 (maximum dead time), which the realization of ZVS can be always achieved. However, the parasitic diode of the switches has higher

conduction loss than conduction resistance. The turn-on moment of Q_{2a} should be chosen as t_1 . During interval 3 and 4, the inductor current i_a keeps decreasing, until i_a reach the desired current lower-level i_{a_down} . The next resonant process is beginning during interval 5. Q_{2a} is turned off at t_3 , then the output capacitors C_{oss} of Q_{1a} is fully discharged to zero, and the diode D_{1a} is conducted at t_4 . Then, Q_{1a} can be turned on during interval 6, which ZVS can be achieved. The TCM operation analysis to other switching cycles is the same.

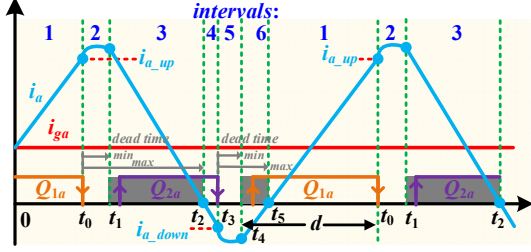


Fig. 2. Inductor current waveform and the different intervals within several switching cycles.

The detailed quantitative calculation process is as follows. The inductor current variation between t_0 and t_3 , and t_3 and t_0 are the opposite. Meanwhile, the dead time (intervals 2 and 5) is so small that can be neglected. The inductor current ripple can be calculated as

$$\begin{cases} i_{a_t3} - i_{a_t0} = (-V_{dc}/2 - v_a)(1 - d)/f_{sw}/L \\ i_{a_t0} - i_{a_t3} = (V_{dc}/2 - v_a)d/f_s/L \end{cases} \quad (1)$$

where d and f_{sw} are the duty ratio and switching frequency, respectively. By simplifying equation (1), the switching frequency can be expressed as

$$f_{sw} = \frac{(V_{dc}/2 - v_a)(V_{dc}/2 + v_a)}{LV_{dc}(i_{a_up} - i_{a_down})} \quad (2)$$

The upper-level and lower-level inductor current can be calculated as

$$\begin{cases} i_{a_up} = 2i_{ga} + i_{bias} \\ i_{a_down} = -i_{bias} \end{cases} \quad (3)$$

where i_{bias} is the bias current to charge/discharge the output capacitors C_{oss} of the switching components, which is discussed in Section IV. Substituting (3) into (2), the switching frequency f_{sw} can be given by

$$f_{sw} = \frac{(V_{dc}/2 - v_a)(V_{dc}/2 + v_a)}{2LV_{dc}(i_{ga} + i_{bias})} \quad (4)$$

Similarly, for the situation that i_{ga} is below zero, the analysis is the same, and the corresponding switching frequency f_{sw} is given by

$$f_{sw} = \frac{(V_{dc}/2 - v_a)(V_{dc}/2 + v_a)}{2LV_{dc}(-i_{ga} + i_{bias})} \quad (5)$$

B. Single Conventional DCM Operation Analysis

DCM can be controlled with a constant switching frequency compared to the TCM operation. Meanwhile, the realization of ZCS turn-on, ZVS turn-off, and valley switching (VS) can reduce the switching loss. However, the current ripple is higher, which causes more conduction loss. Similarly, taking phase a whose load current is above 0 as an example, Fig. 3 shows the

switching waveforms under DCM operation. v_{Q1a_ds} and v_{Q2a_ds} are the drain-source voltage of Q_{1a} and Q_{2a} . Assuming that the valley switching (VS) is achieved in each switching cycle, and the converter operates with a fixed switching frequency for the convenient analysis. Q_{1a} is conducted and the inductor current increases linearly. At t_0 , the inductor current i_a is equal to the desired current upper-level i_{a_up} . Q_{1a} is turned off, then the output capacitors C_{oss} of Q_{1a} and Q_{2a} are charged and discharged, respectively. At t_1 , the output capacitors C_{oss} of Q_{2a} is fully discharged to zero and ZVS of Q_{2a} can be achieved. Meanwhile, Q_{2a} should be turned on at this moment to reduce the conduction loss. The inductor current i_a starts to decrease and becomes zero at t_2 . Q_{2a} is turned off at this moment. Therefore, the ZVS turn-off is achieved. Then, i_a oscillates around zero, until Q_{1a} is turned on at t_4 (the valley of v_{Q1a_ds}). The ZCS turn-on is also achieved at t_4 . The detailed quantitative calculation process is as follows.

With a constant switching cycle T_{sw} , the average inductor current i_{ga} can be expressed as

$$i_{ga} = i_{a_up}(T_{on_DCM} + T_{off_DCM})/2T_{sw} \quad (6)$$

where T_{on_DCM} and T_{off_DCM} are the ON-time and OFF-time of the switches, respectively. i_{a_up} is the maximum value of inductor current i_a , which can be given by

$$\begin{cases} T_{on_DCM} = d_{on}T_{sw} \\ T_{off_DCM} = i_{a_up}L/(V_{dc}/2 + v_a) \\ i_{a_up} = (V_{dc}/2 - v_a)d_{on}T_{sw}/L \end{cases} \quad (7)$$

where d_{on} is the turn-on duty ratio of Q_{1a} . Substituting (7) into (6), d_{on} is given by

$$d_{on} = \sqrt{i_{ga}} \sqrt{\frac{L(0.5V_{dc} + v_a)}{0.5V_{dc}T_{sw}(0.5V_{dc} - v_a)}} \quad (8)$$

From these equations, the peak inductor current i_{a_up} can be expressed as

$$i_{a_up} = \frac{0.5V_{dc} - v_a}{L} T_{sw} d_{on} \quad (9)$$

Meanwhile, the amplitude of inductor current rise and fall is the same in a switching cycle. The turn-off duty ratio d_{off} , and the sum of turn-off and turn-on duty ratio d_{all} can be written as

$$\begin{cases} d_{off} = \frac{0.5V_{dc} - v_a}{0.5V_{dc} + v_a} d_{on} \\ d_{all} = d_{on} + d_{off} \end{cases} \quad (10)$$

Similarly, for the situation that i_{ga} is below zero, the analysis is the same, and d_{on} and d_{off} are given by

$$\begin{cases} d_{on} = \sqrt{-i_{ga}} \sqrt{\frac{L(0.5V_{dc} - v_a)}{0.5V_{dc}T_{sw}(0.5V_{dc} + v_a)}} \\ d_{off} = \frac{0.5V_{dc} + v_a}{0.5V_{dc} - v_a} d_{on} \end{cases} \quad (11)$$

If d_{all} is equal to 1, critical conduction mode (CRM) operation is achieved rather than DCM. And continuous conduction mode (CCM) operates when d_{all} is above 1, which is not suitable because the soft switching is lost.

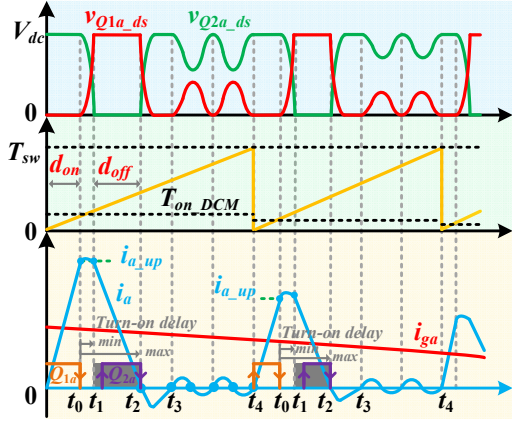


Fig. 3. Switching waveforms under DCM operation.

The switching frequency variation under TCM and the duty ratio variation under DCM at different loads can be plotted in Fig. 4. Based on the above analysis of TCM, ZVS can be achieved easily. However, Fig. 4 (a) shows that the switching frequency under TCM is more than MHz near the zero crossing of load current, and increases sharply at the lighter loads, which is always above 500 kHz at 10% load. This causes significant turn-off loss even if the current ripple is small. On the contrary, the duty ratio under DCM is small near the zero crossing of load current and decreases at the lighter loads with a constant switching frequency. Therefore, TCM can be changed to DCM for limiting the switching frequency at light loads or zero crossing of load current. Meanwhile, the constant switching frequency and soft switching (such as ZCS turn-on, ZVS turn-off, and VS) can be achieved under DCM operation to reduce switching losses. However, the maximum d_{all} is above 1 at 3.3 kW as Fig. 4 (b) shows, which means that CCM is achieved during the angle range to cause soft switching loss. Therefore, the maximum power under DCM operation should be limited, which is discussed in Section III. Meanwhile, consistent VS is difficult to be achieved. Because the fixed turn-on point leads to VS failure, which causes unpredictable output current distortion and turn-on switching loss.

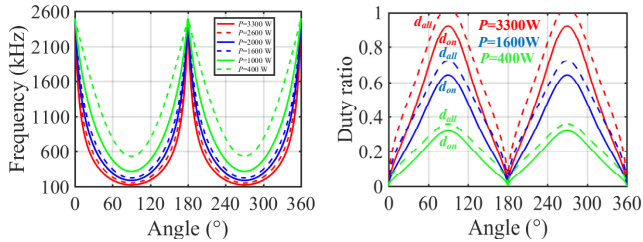


Fig. 4. Variation waveforms at different loads.

III. VARIABLE SWITCHING FREQUENCY CONTROL UNDER DCM OPERATION

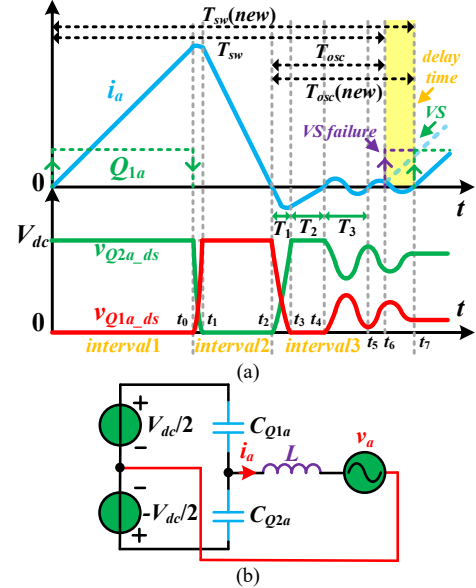
In this Section, the analysis of the variable switching frequency control under DCM operation to achieve consistent VS is discussed with an inverter interfacing 400 V dc and three-phase 110 V RMS ac. Assume that the circuit parameters are

given as listed in Table I. Because DCM is designed to operate at light load to improve light efficiency, the maximum power under DCM operation is assumed to be 3 kW because d_{all} is very close to 1.

TABLE I
CIRCUIT PARAMETERS

Item	Parameter
Grid line to line voltage v_x	190 V RMS
DC voltage V_{dc}	400 V
Rated Power P_{max}	3.3 kW
Maximum Power (DCM)	3 kW
Inductance L	10 μ H
Power factor PF	1
Bias current I_{bias} (TCM)	2 A
Switching frequency T_{sw} (DCM)	150 kHz

To address the aforementioned issues of DCM operation, a variable switching frequency control is presented to achieve consistent VS. One assumption for the following analysis is added that i_x becomes zero, and v_{Qx_ds} is located in the valley at the end of T_{sw} .

Fig. 5. DCM operation achieving VS. (a) Variable switching frequency control process. (b) Resonance process during T_{osc} .

Still taking phase a whose load current is above 0 as an example, the variable switching frequency control process during one switching cycle is plotted in Fig. 5 (a). There are three types of resonance during interval 3, which are named T_1 , T_2 , and T_3 , respectively. The resonance time T_{osc} can be expressed as

$$T_{osc} = T_1 + T_2 + nT_3 \quad (12)$$

where n is usually not an integer number. Therefore, the turn-on switching point of Q_{1a} occurs at non-zero of the inductor current, which causes VS failure, as shown by the purple dashed line in Fig. 5 (a). However, n can be equal to an integer with the variable switching frequency, the inductor current always becomes zero at the end of $T_{osc}(new)$, and v_{Q1a_ds} oscillates to the valley. The VS can be achieved. Therefore, the resonance process of Q_{1a} and Q_{2a} during interval 3 should be analyzed. Fig.

5 (b) shows the Thevenin's simplified circuit. C_{Q1a} and C_{Q2a} are the C_{oss} of Q_{1a} and Q_{2a} . According to the equivalent circuit, the resonant process during T_1 can be expressed as

$$\begin{cases} i_a(t_2) = 0, v_{Q1a_ds}(t_2) = V_{dc}, v_{Q2a_ds}(t_2) = 0 \\ v_{Q1a_ds}(t_3) = 0, v_{Q2a_ds}(t_3) = V_{dc} \\ v_{Q2a_ds} - 0.5V_{dc} - v_a = L \frac{di_a}{dt} \\ C_{Q1a} \frac{dv_{Q1a_ds}}{dt} - C_{Q2a} \frac{dv_{Q2a_ds}}{dt} = i_a \end{cases} \quad (13)$$

Therefore, T_1 and $i_a(t_3)$ can be given by

$$\begin{cases} T_1 = \frac{1}{w_r} \arccos\left(\frac{v_a - 0.5V_{dc}}{v_a + 0.5V_{dc}}\right) \\ i_a(t_3) = -\sqrt{\frac{2C_{oss}}{L}} (0.5V_{dc} + v_a) \sin(w_r T_1) \end{cases} \quad (14)$$

where

$$w_r = \frac{1}{\sqrt{2C_{oss}L}} \quad (15)$$

where C_{oss} is the output capacitor of switches from datasheet. However, the extra parasitic capacitances caused by the driving circuit and the PCB may also contribute to the total capacitance of switches. The actual value of C_{oss} is bigger than the datasheet.

After v_{Q1a_ds} becomes zero, i_a starts to flow through the body diode of Q_{1a} . During T_2 , v_{Q1a_ds} and v_{Q2a_ds} are clamped to zero and V_{dc} , respectively. During T_2 , i_a can be expressed as

$$i_a(t) = \frac{(0.5V_{dc} - v_a)}{L} (t - t_3) + i_a(t_3) \quad (16)$$

At t_4 , i_a becomes zero, and the output capacitors C_{oss} of Q_{1a} and Q_{2a} will be charged and discharged, respectively, at the end of the block period. T_2 can be given by

$$T_2 = L \frac{i_a(t_3)}{v_a - 0.5V_{dc}} \quad (17)$$

In this paper, the resonance process during T_3 is regarded as a pure LC oscillation. Therefore, T_3 is assumed to be constant and approximated by [28]

$$T_3 \approx 2\pi\sqrt{2LC_{oss}} \quad (18)$$

The analysis is the same when i_{ga} is below zero. The aforementioned formula of resonance cycle T_1 and T_2 can be summarized as

$$\begin{cases} T_1 = \frac{1}{w_r} \arccos\left(\frac{|v_a| - 0.5V_{dc}}{|v_a| + 0.5V_{dc}}\right) \\ T_2 = \sqrt{LC_{oss}} \frac{0.5V_{dc} + |v_a|}{0.5V_{dc} - |v_a|} \sin(w_r T_1) \end{cases} \quad (19)$$

Therefore, during T_{sw} , n can be given by

$$n = \frac{(1 - d_{on} - d_{off})T_s - T_1 - T_2}{T_3} \quad (20)$$

Usually, n is not an integer. Therefore, n should be round down, and the new switching frequency $T_{sw}(new)$ can be calculated as

$$T_s(new) = T_s(d_{on} + d_{off}) + T_1 + T_2 + (\text{floor}(n) + 1)T_3 \quad (21)$$

where the function $\text{floor}()$ represents the symbol of the round down. As shown by the green dashed line in Fig. 5 (a), by delaying the part-time of resonance cycle T_3 backward, VS can always be achieved at the end of $T_{sw}(new)$. The resonance cycle T_3 is so small that the deviation can be neglected.

According to circuit parameters in Table I, equations (10), (20), and (21), the peak inductor current, variable switching frequency, and variable numbers of n during half line cycle at 3 kW can be plotted in Fig. 6 (a). It can be seen that the number

of n increases as load decreases, which ensures that additional resonance cycle T_3 can also be avoided, as Fig. 6 (b) shows. Therefore, the unnecessary circulation losses are reduced.

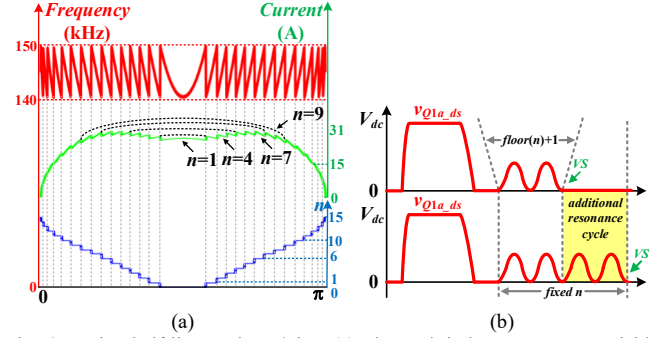


Fig. 6. During half line cycle at 3 kW (a) The peak inductor current, variable switching frequency, and numbers of n . (b) resonance waveforms of v_{Q1a_ds} .

IV. PROPOSED MIXED TCM/DCM OPERATION BASED POWER LOSS ANALYSIS

What is the optimum changing modulation point (modulation changes from TCM to DCM) to achieve high efficiency at full range loads? It is important to improve the overall efficiency performance. The power loss of single TCM and single DCM operation are analyzed as follows, and calculated to find the tradeoff between load current and efficiency to determine the optimum changing point at different loads.

A. Power Loss Analysis

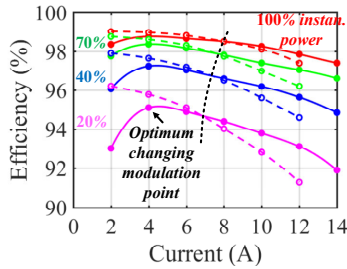
The losses are mainly consisted of four sources: switching loss (including MOSFET body diode conduction loss), conduction loss of switches, copper loss, and core loss of inductor. Because ZVS can be achieved under TCM operation, turn-on loss can be neglected. Only turn-off switching loss is calculated. However, under DCM operation, VS is not ZVS in the strict sense, and turn-on losses still exist due to the non-zero valley drain-source voltage, as Fig. 5 (a) shows. Therefore, turn-on losses should be calculated under DCM operation. The inductor current changes its direction, and the body diode of switches conducts during the dead time, which should also be calculated. The conduction loss in the switches is independent of the switching frequency [29], which has a strong correlation with the drain-source current (inductor rms current). And the core loss is estimated by the Generalized Steinmetz Equation (GSE) [30]. The variable switching frequency and core flux density are taken into account to supply a more accurate core loss value. As for the copper losses for the inductor, which consist of dc and ac losses. dc losses are simply the multiplication of dc resistance and inductor rms current. However, it is complicated to calculate the ac losses accurately due to the variable switching frequency. In this design, the ac resistances and inductor rms current from 100 to 500 kHz (TCM) and from 140 to 150 kHz (DCM) are measured offline by the impedance analyzer and FFT of the oscilloscope. Therefore, the ac losses can be gotten accurately.

Fig. 7 (a) shows the calculated efficiency as a function of load current under single TCM (solid line) and DCM (dashed line) operation, respectively. At fixed power, the efficiency increases until that load current is equal to 4 A under TCM operation. However, the efficiency decreases as load current increases above 4 A, because the turn-off and conduction losses start to increase due to the higher inductor current ripple. Meanwhile, as load current decreases below 4 A, the turn-off losses and core losses of inductor are much high due to the significantly increasing switching frequency. Under DCM operation, the efficiency keeps decreasing as load current increases, due to the high inductor current ripple. Therefore, the turn-off and conduction losses are much more than TCM operation with higher load current. However, the efficiency performs better than TCM at lower load current (around 7 A). Because the switching losses are small with a lower switching frequency.

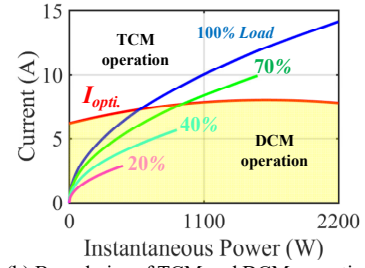
The optimum changing modulation point is determined by the intersection of efficiency. By connecting these intersection efficiency points into a line, it is noticed that the optimum changing modulation points are located within a narrow range of load current, which is easy to synthesize into a functional expression. In this design, the function between optimum changing point (load current) and single-phase instantaneous power can be given by

$$I_{opti.} = -7.089e^{-7}P_{instan.}^2 + 2.283e^{-3}P_{instan.} + 6.167 \quad (22)$$

where $I_{opti.}$ is the calculated the optimum changing point of load current, and $P_{instan.}$ is the single-phase instantaneous power. Therefore, the boundaries of TCM and DCM operation can be gotten as Fig. 7 (b) shows. Taking the full load situation (blue line) as an example, the operation should be changed from TCM to DCM when load current is below about 7 A, which is also the corresponding current to the efficiency intersection of single TCM and single DCM at 25% instantaneous power. Therefore, the overall efficiency can be improved, which combines the better performance of DCM and TCM operation at light and heavy loads, respectively. It can be seen that DCM always operates when power is lower than 40% percent. This shows the actual operating power range of the converter that only operates under DCM, which is coincidental with the fact that DCM is usually employed at low power situation.



(a) Calculated efficiency under single TCM (solid line) and DCM (dashed line) operation.



(b) Boundaries of TCM and DCM operation.

Fig. 7. At different instantaneous powers for single-phase.

B. Mixed TCM/DCM Operation

Based on the aforementioned power loss analysis, a mixed TCM/DCM operation control is proposed to improve the light efficiency and narrow switching frequency range. Fig. 8 shows the mixed TCM/DCM operation waveforms during half line cycle. The optimum changing modulation points are gotten from Fig. 7. At full load, the dwell time of TCM operation is larger than DCM that reduces the inductor rms current to achieve lower conduction losses. While at 60% load, the dwell time of DCM operation is larger than TCM that reduces the switching frequency to achieve low turn-off losses.

The power distribution for a 3.3 kW three-phase inverter under different modulation is shown in Fig. 9. Since TCM has the highest switching frequency, the switching losses are the highest among these modulations. Meanwhile, the conduction losses are the highest under DCM operation, due to the biggest inductor current ripple, which increases the inductor rms current. The lowest switching and conduction losses can be achieved under the mixed TCM/DCM operation. Because the limited variable switching frequency range with small load current causes low switching losses, and low conduction losses are achieved due to the lower inductor current ripple with big load current.

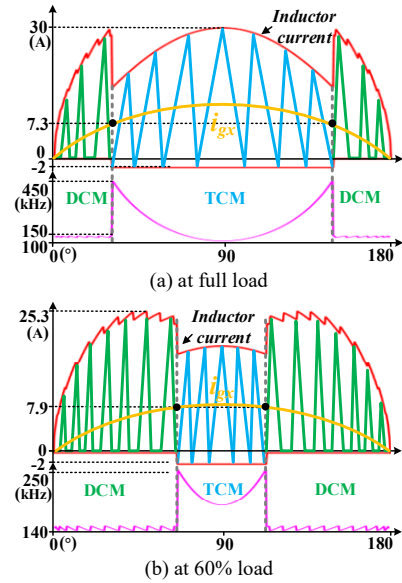


Fig. 8. Mixed TCM/DCM operation during half line cycle.

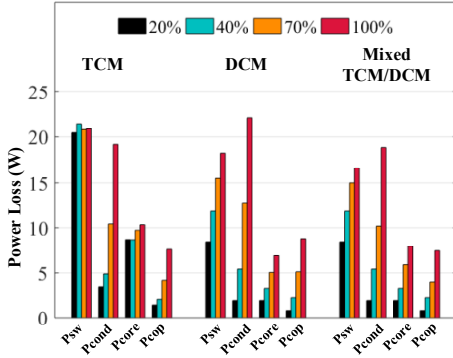


Fig. 9. Power loss distribution under different modulation at 20%, 40%, 70%, and 100% of inverter rated power.

V. DESIGN CONSIDERATION

In this section, the design considerations of filter parameters, and the bias current under TCM are discussed. The minimum switching frequency is set as 100 kHz to fully utilize the fast switching speed of SiC MOSFETs.

For TCM, the inverter side inductor L not only influences the switching frequency but also affects the design of I_{bias} and the dead time t_d . For DCM, L determines the max value of d_{all} at the setting switching frequency. Thus, they should be designed together based on the most difficult situation. It can be proved that the worst-case occurs when v_x is at its maximum voltage (angle is 0°) at full load. Because the switching frequency variation range is narrow under DCM operation, the switching frequency is considered as constant 150 kHz (d_{all} is bigger) for analyzing easily. Still taking phase a whose load current is above 0 as an example. The ZVS resonant process of Q_{1a} around t_3 (in Fig. 2) is analyzed. Fig. 10 (a) shows the equivalent circuit during the dead time before Q_{1a} is turned on. C_{Q1a} and C_{Q2a} are the C_{oss} of Q_{1a} and Q_{2a} . The ZVS resonant process starts at t_3 . According to the equivalent circuit, the resonant process can be expressed as

$$\begin{cases} v_{Q1a,ds} + v_{Q2a,ds} = V_{dc}, v_{Q1a,ds}(t_3) = V_{dc} \\ i_a(t_3) = -I_{bias} \\ C_{Q1a} \frac{dv_{Q1a,ds}}{dt} - C_{Q2a} \frac{dv_{Q2a,ds}}{dt} = i_a \\ L \frac{di_a}{dt} + v_a - v_{Q2a,ds} = 0 \end{cases} \quad (23)$$

The waveform of the ZVS realization is shown in Fig. 10 (b) according to (23). It can be seen that the resonant process starts at t_3 and ends after a time duration of minimum dead time. The inductor current i_a decreases linearly after the resonant process and becomes zero at maximum dead time. The ZVS for Q_{1a} can be achieved if the driving signal is applied in the yellow marked area. Otherwise, C_{Q1a} will be recharged as i_a becomes positive. The area should be small as possible to reduce the circulation loss.

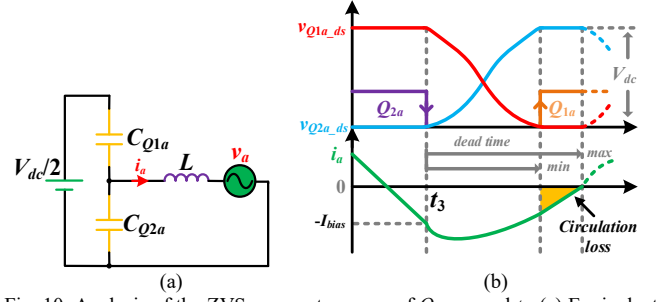


Fig. 10. Analysis of the ZVS resonant process of Q_{1a} around t_3 . (a) Equivalent circuit. (b) Resonant waveform.

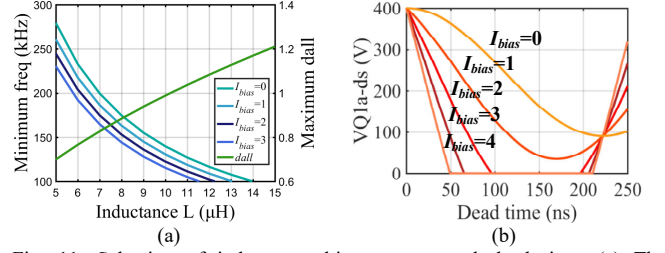


Fig. 11. Selection of inductance, bias current, and dead time. (a) The relationship that the minimum switching frequency versus different L and I_{bias} at 3.3 kW under TCM operation and the maximum d_{all} with different L at 3 kW under DCM operation. (b) Resonant voltage waveform of $v_{Q1a,ds}$ at different bias current using $10 \mu H$ L .

TABLE II
DEAD TIME SELECTION WITH DIFFERENT BIAS CURRENTS

I_{bias} (A)	L (μH)	t_{dmin} (ns)	t_{dmax} (ns)
0	14	N/A	N/A
1	13	N/A	N/A
2	12.2	97	217
3	11.5	64	224

The relationship between the minimum frequency and the inductance L versus different bias currents at 3.3 kW under TCM operation and the maximum d_{all} with different L at 3 kW under DCM operation is shown in Fig. 11 (a). One SiC MOSFET is used in each phase-leg, whose output capacitor C_{oss} is 250 pF considering the extra parasitic capacitances caused by the driving circuit and the PCB. By substituting the parameters obtained from Fig. 11 (a) into (23), the dead time range can be calculated and given in Table II. When L is $10 \mu H$, the resonant voltage waveform of $v_{Q1a,ds}$ at different I_{bias} is illustrated in Fig. 11 (b). It can be seen that $v_{Q1a,ds}$ cannot drop to zero when I_{bias} is 0 or 1 A. However, C_{Q1a} can be fully discharged when I_{bias} is greater than 2 A. When I_{bias} is equal to 2 A, the dead time can be set between 90 ns and 190 ns. Considering the turn-on and turn-off time of the SiC devices and the tolerance of the propagation delay of the driving circuits, I_{bias} is set as 2 A. L is designed as $10 \mu H$. The dead time is set to 100 ns.

VI. SIMULATION AND EXPERIMENTAL VERIFICATION

In order to verify the performance of the proposed control, simulation, and experimental results are carried out in this Section. The specification and the parameters are obtained from Section IV and given in Table III.

Fig. 12 shows the simulation waveform in a line cycle at full load. v_o is the voltage of the neutral-point dc-bus. The inductor

current ripple is consistent with the above discussion. For example, in phase a , the bias current is maintained well at 2 A or -2 A under TCM operation. Therefore, ZVS can be achieved for all the switches. Under DCM operation, the switching frequency f_{sw_a} is limited from 140-150 kHz to avoid the sharply increasing switching frequency of TCM. Although the current ripple at the inverter side is high, the current ripple at the grid side is small.

Fig. 13 shows the valley switching (VS) waveforms at 60% load. VS is achieved well by the variable switching frequency under DCM operation to change the numbers of n . It can be seen that the integer number of n increases as load increases, and the valley value of the drain-source voltage Q_{1a_ds} is further away from zero. Therefore, the turn-on losses still exist. The reason is the limited maximum switching frequency 150 kHz under DCM operation, which causes the numbers of resonance cycle T_3 to only increase but not decrease. Actually, the turn-on losses can be eliminated by increasing the switching frequency further under DCM operation. Due to the length of the article, the optimization design will be discussed in the future work.

TABLE III
SPECIFICATION AND THE PARAMETERS OF THE INVERTER

Item	Parameter	Item	Parameter
DC voltage V_{dc}	400 V	Grid line voltage v_x	110 V RMS
Rated power P_{max}	3.3 kW	Power Factor	1
Inductance L	10 μ H	Bias current I_{bias}	2 A
Capacitance C	4.7 μ F	Dead time t_d	100 ns
DC capacitor C_{dc}	440 μ F	Max freq (DCM)	150 kHz
Min freq (TCM)	100 kHz	Max freq (TCM)	500 kHz

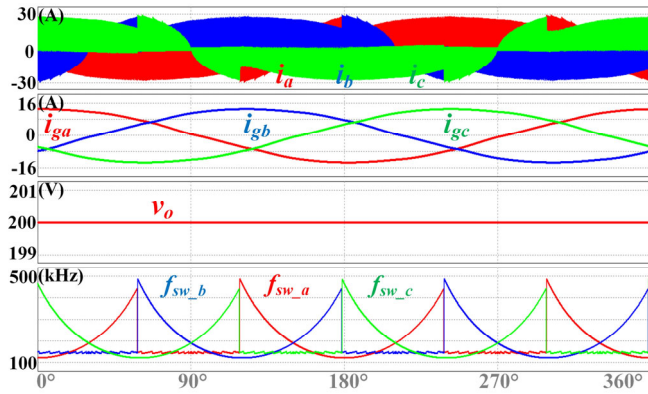


Fig. 12. Simulation waveform in a line cycle at 400-V dc full load.

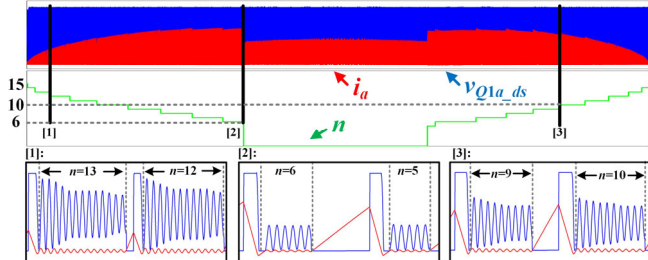


Fig. 13. Valley switching waveforms at 60% load.

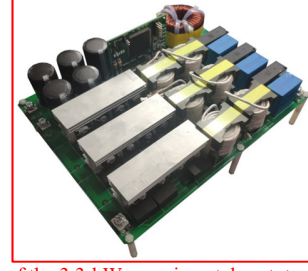


Fig. 14. Photograph of the 3.3-kW experimental prototype.

Fig. 14 shows the photograph of the experimental prototype, which is fabricated using six SiC MOSFETs C3M0045065K (650 V, 45 m Ω). Three inverter-side inductors are built with ferrite cores and Litz wire to reduce the high frequency power loss. TMS320F28374S and AGRV2K (DSP+CPLD) are chosen as the digital controller. The sampling and control frequencies are set as 50 kHz.

Since the three-phase voltages and currents have similar waveforms, only one phase is discussed in detail. Fig. 15 shows the experimental waveforms at from 5% to 100% loads during several line cycles. The switching frequency curve f_{sw_b} is generated by the digital to analog converter (DAC) in the DSP. The dwell time of DCM operation increases as load decreases to improve the light load efficiency. The neutral-point voltage fluctuation v_o is shown in Fig. 16, which is consistent with the simulation. The bias current is still tightly controlled. Only a little error is mainly caused by the sampling inaccuracy.

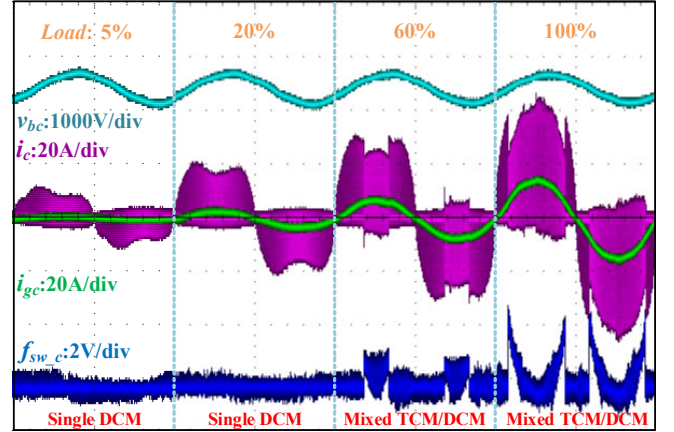


Fig. 15. Experimental waveforms at different loads.

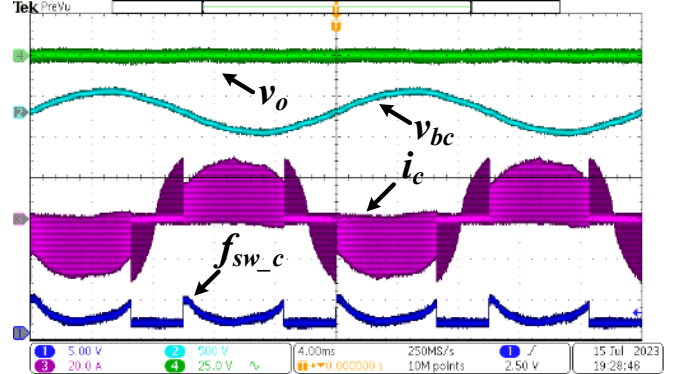


Fig. 16. Steady-state waveforms of phase c at full load in line cycles.

For phase a (phases b and c are the same), Q_{1a} and Q_{2a} can be achieved ZVS only when the inductor current flow out or into the middle point of phase-leg, respectively. It can be verified in Fig. 17 (a)-(d). For the top switch Q_{1a} , in Fig. 17 (a) and (b), the minimum value of i_a is around -2 A, which ensures that the drain-to-source voltage v_{Q1a_ds} decreases to zero before the driving signal v_{Q1a_gs} becomes high. For the bottom switch Q_{2a} , all the peak currents are greater than 2 A in Fig. 17 (c) and (d). It can be seen that at any position, the drain-to-source voltage v_{Q2a_ds} decreases to zero before the driving signal v_{Q2a_gs} becomes high. Therefore, full-range ZVS can be achieved for all the switches in TCM operation.

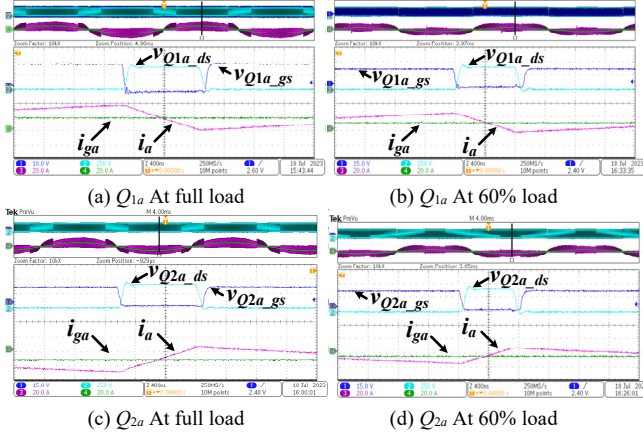


Fig. 17. ZVS realization of the top switch Q_{1a} and the bottom switch Q_{2a} in TCM operation.

Fig. 18 shows the valley switching of the top switch Q_{1a} at different position. It can be seen that the valley switching can be achieved well even the resonance cycles are from 2 to 15, and the current is nearly zero before Q_{1a} is turned on. Therefore, ZCS turn-on can be verified. The dynamic response of the inverter is verified and shown in Fig. 19. The load step changes from 60% to full load. It can be seen that the bias current can always be kept at the designed value both before and after the transient under TCM operation. Therefore, ZVS realization can always be guaranteed.

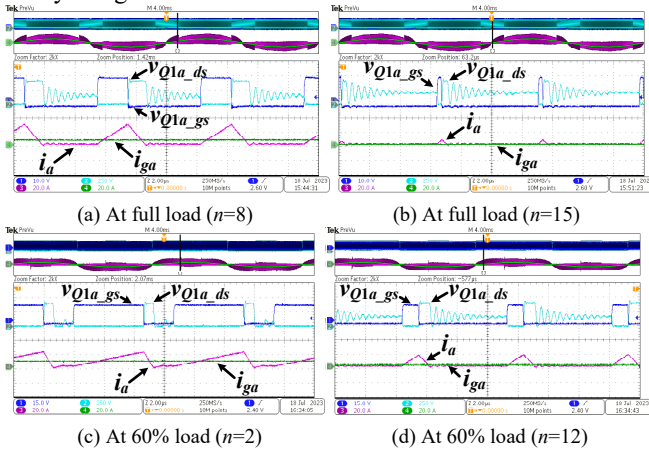


Fig. 18. Valley switching of the top switch Q_{1a} at different positions in DCM operation.

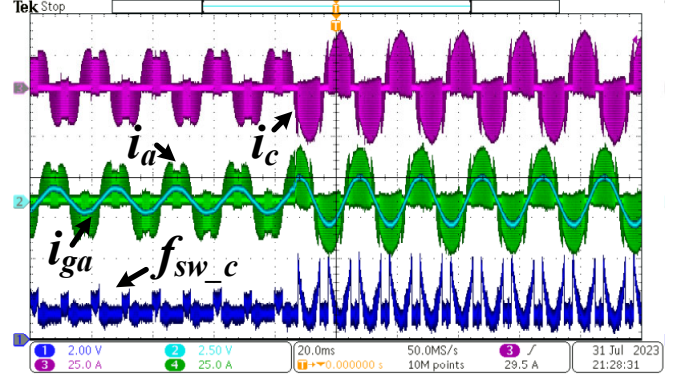


Fig. 19. Dynamic response during load step change from 60% to full load.

The tested inverter efficiency comparison for different operations: TCM, DCM, and mixed TCM/DCM at different loads are presented in Fig. 20, which is obtained by the WT1806E power analyzer. The light efficiency improvement is significant under mixed TCM/DCM operation compared to TCM by 0.55% to 3.9%. This is because the switching frequency is limited at light loads or zero crossing of load current by changing control from TCM to DCM. Especially, the most part of the losses is the switching loss. The conduction loss is relatively small.

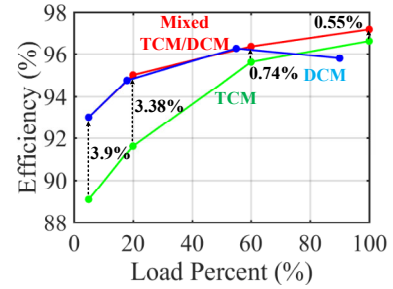


Fig. 20. The tested inverter efficiency comparison for different operations: TCM, DCM, and mixed TCM/DCM at different loads.

VII. CONCLUSION

This paper proposes a variable switching frequency control under mixed TCM/DCM operation to improve the light load efficiency and limited switching frequency variation. The loss under single TCM and DCM is analyzed to optimize the changing modulation point. The operating principle, ZVS realization under TCM, and consistent VS under DCM are analyzed in detail.

Whether under TCM or DCM, instead of using the ZCD circuit, the variable switching frequency can be easily calculated in a digital controller without any high-frequency sensor or auxiliary circuit. The switching frequency is limited at light loads or zero crossing of load current by changing the operation from TCM with variable frequency to DCM with variable frequency. Therefore, the switching loss can be greatly reduced. Meanwhile, owing to the high switching frequency and low inductance of the filter, the power density and the dynamic response can be significantly increased. Experiments with the proposed control validate that substantial light load efficiency improvement is achieved resulting in enhanced

weighted efficiency, and the superior characteristics of the wide band-gap power devices can be fully exploited.

REFERENCES

- [1] R. Li and D. Xu, "A Zero-Voltage Switching Three-Phase Inverter," *IEEE Trans. Power Electron.*, vol. 29, no. 3, pp. 1200-1210, March 2014.
- [2] R. Gurunathan and A. K. S. Bhat, "Zero-Voltage Switching DC Link Single-Phase Pulsewidth-Modulated Voltage Source Inverter," in *IEEE Transactions on Power Electronics*, vol. 22, no. 5, pp. 1610-1618, Sept. 2007, doi: 10.1109/TPEL.2007.904169.
- [3] Y. Chen et al., "A ZVS Grid-Connected Full-Bridge Inverter With a Novel ZVS SPWM Scheme," in *IEEE Transactions on Power Electronics*, vol. 31, no. 5, pp. 3626-3638, May 2016, doi: 10.1109/TPEL.2015.2456032.
- [4] Xiaoming Yuan and I. Barbi, "Analysis, designing, and experimentation of a transformer-assisted PWM zero-voltage switching pole inverter," in *IEEE Transactions on Power Electronics*, vol. 15, no. 1, pp. 72-82, Jan. 2000, doi: 10.1109/63.817365.
- [5] W. Yu, J. -S. Lai and S. -Y. Park, "An Improved Zero-Voltage Switching Inverter Using Two Coupled Magnetics in One Resonant Pole," in *IEEE Transactions on Power Electronics*, vol. 25, no. 4, pp. 952-961, April 2010, doi: 10.1109/TPEL.2009.2030197.
- [6] C. -M. Wang, C. -H. Su, M. -C. Jiang and Y. -C. Lin, "A ZVS-PWM Single-Phase Inverter Using a Simple ZVS-PWM Commutation Cell," in *IEEE Transactions on Industrial Electronics*, vol. 55, no. 2, pp. 758-766, Feb. 2008, doi: 10.1109/TIE.2007.911925.
- [7] X. Huang, F. C. Lee, Q. Li, and W. Du, "High-Frequency High-Efficiency GaN-Based Interleaved CRM Bidirectional Buck/Boost Converter with Inverse Coupled Inductor," *IEEE Trans. Power Electron.*, vol. 31, no. 6, pp. 4343-4352, June 2016.
- [8] B. Su, J. Zhang and Z. Lu, "Totem-Pole Boost Bridgeless PFC Rectifier With Simple Zero-Current Detection and Full-Range ZVS Operating at the Boundary of DCM/CCM," *IEEE Trans. Power Electron.*, vol. 26, no. 2, pp. 427-435, Feb. 2011.
- [9] Q. Zhang, H. Hu, D. Zhang, X. Fang, Z. J. Shen and I. Batarseh, "A Controlled-Type ZVS Technique Without Auxiliary Components for the Low Power DC/AC Inverter," *IEEE Trans. Power Electron.*, vol. 28, no. 7, pp. 3287-3296, July 2013.
- [10] D. Bortis, D. Neumayr and J. W. Kolar, "ηp-Pareto optimization and comparative evaluation of inverter concepts considered for the GOOGLE Little Box Challenge," *2016 IEEE 17th Workshop on Control and Modeling for Power Electronics (COMPEL)*, 2016, pp. 1-5.
- [11] D. Jiang and F. Wang, "Variable Switching Frequency PWM for Three-Phase Converters Based on Current Ripple Prediction," *IEEE Trans. Power Electron.*, vol. 28, no. 11, pp. 4951-4961, Nov. 2013.
- [12] J. Chen, D. Sha and J. Zhang, "Current Ripple Prediction and DPWM-Based Variable Switching Frequency Control for Full ZVS Range Three-Phase Inverter," in *IEEE Transactions on Industrial Electronics*, vol. 68, no. 2, pp. 1412-1422, Feb. 2021, doi: 10.1109/TIE.2020.2967741.
- [13] J. Chen, D. Sha, J. Zhang and X. Liao, "An SiC MOSFET Based Three-Phase ZVS Inverter Employing Variable Switching Frequency Space Vector PWM Control," in *IEEE Transactions on Power Electronics*, vol. 34, no. 7, pp. 6320-6331, July 2019, doi: 10.1109/TPEL.2018.2874036.
- [14] Z. Huang, Z. Liu, F. C. Lee and Q. Li, "Critical-Mode-Based Soft-Switching Modulation for High-Frequency Three-Phase Bidirectional AC-DC Converters," in *IEEE Transactions on Power Electronics*, vol. 34, no. 4, pp. 3888-3898, April 2019, doi: 10.1109/TPEL.2018.2854302.
- [15] N. Haryani, B. Sun and R. Burgos, "A novel soft switching ZVS, sinusoidal input boundary current mode control of 6-switch three phase 2-level boost rectifier for active and active + reactive power generation," *2018 IEEE Applied Power Electronics Conference and Exposition (APEC)*, San Antonio, TX, USA, 2018, pp. 8-15.
- [16] B. Fan, Q. Wang, R. Burgos, A. Ismail and D. Boroyevich, "Adaptive Hysteresis Current Based ZVS Modulation and Voltage Gain Compensation for High-Frequency Three-Phase Converters," in *IEEE Transactions on Power Electronics*, vol. 36, no. 1, pp. 1143-1156, Jan. 2021, doi: 10.1109/TPEL.2020.3002894.
- [17] M. Kaufmann, A. Tüysüz and J. W. Kolar, "New optimum modulation of three-phase ZVS triangular current mode GaN inverter ensuring limited switching frequency variation," *8th IET International Conference on Power Electronics, Machines and Drives (PEMD 2016)*, Glasgow, UK, 2016, pp. 1-6, doi: 10.1049/cp.2016.0135.
- [18] D. Zhang, Q. Zhang, H. Hu, A. Grishina, J. Shen and I. Batarseh, "High efficiency current mode control for three-phase micro-inverters," *2012 Twenty-Seventh Annual IEEE Applied Power Electronics Conference and Exposition (APEC)*, Orlando, FL, USA, 2012, pp. 892-897, doi: 10.1109/APEC.2012.6165924.
- [19] A. Amirahmadi et al., "Hybrid ZVS BCM Current Controlled Three-Phase Microinverter," in *IEEE Transactions on Power Electronics*, vol. 29, no. 4, pp. 2124-2134, April 2014.
- [20] M. Valentini, A. Raducu, D. Sera and R. Teodorescu, "PV inverter test setup for European efficiency, static and dynamic MPPT efficiency evaluation," *2008 11th International Conference on Optimization of Electrical and Electronic Equipment, Brasov, Romania*, 2008, pp. 433-438.
- [21] U. Somani, C. Jourdan, A. Amirahmadi, A. Grishina, H. Hu and I. Batarseh, "Phase skipping control to improve light load efficiency of three phase micro-inverters," *2014 IEEE Applied Power Electronics Conference and Exposition - APEC 2014*, Fort Worth, TX, USA, 2014, pp. 2944-2949, doi: 10.1109/APEC.2014.6803723.
- [22] H. Hu, W. Al-Hoor, N. H. Kutkut, I. Batarseh and Z. J. Shen, "Efficiency Improvement of Grid-Tied Inverters at Low Input Power Using Pulse-Skipping Control Strategy," in *IEEE Transactions on Power Electronics*, vol. 25, no. 12, pp. 3129-3138, Dec. 2010.
- [23] S. M. Tayebi, C. Jourdan and I. Batarseh, "Dynamic Dead-Time Optimization and Phase Skipping Control Techniques for Three-Phase Microinverter Applications," in *IEEE Transactions on Industrial Electronics*, vol. 63, no. 12, pp. 7523-7532, Dec. 2016.
- [24] S. M. Tayebi, C. Jourdan and I. Batarseh, "Advanced phase-skipping control with improved efficiency of three-phase micro-inverters," *2015 IEEE Energy Conversion Congress and Exposition (ECCE)*, Montreal, QC, Canada, 2015, pp. 3802-3806, doi: 10.1109/ECCE.2015.7310197.
- [25] S. M. Tayebi and I. Batarseh, "Analysis and Optimization of Variable-Frequency Soft-Switching Peak Current Mode Control Techniques for Microinverters," in *IEEE Transactions on Power Electronics*, vol. 33, no. 2, pp. 1644-1653, Feb. 2018, doi: 10.1109/TPEL.2017.2676097.
- [26] G. Son, Z. Huang and Q. Li, "Light Load Efficiency Improvement for Two-Channel Paralleled Soft-Switching Three-Phase Inverter Using Phase Shedding Control," in *IEEE Transactions on Power Electronics*, vol. 37, no. 9, pp. 10200-10212, Sept. 2022.
- [27] J. Zhang, T. Isobe and H. Tadano, "Model-Based Control for Grid-Tied Inverters Operated in Discontinuous Current Mode With Low Harmonic Current Distortion," in *IEEE Transactions on Power Electronics*, vol. 35, no. 10, pp. 11167-11180, Oct. 2020, doi: 10.1109/TPEL.2020.2978871.
- [28] Isobe, T., Kato, K., Kojima, N., & Shimada, R. (2014). Soft-switching single-phase grid-connecting converter using DCM operation and a turn-off snubber capacitor. *IEEE Transactions on Power Electronics*, 29(6), 2922-2930.
- [29] Y. Xia and R. Ayyanar, "Optimal variable switching frequency scheme to reduce combined switching loss and inductor core loss of single phase grid connected inverter," *2015 IEEE Energy Conversion Congress and Exposition (ECCE)*, Montreal, QC, Canada, 2015, pp. 1534-1540.
- [30] C. McLyman, *Transformer and Inductor Design Handbook*, Third Edition, ser. Electrical and Computer Engineering Series. Taylor & Francis, 2004.